






Nodeless superconductivity in the topological nodal-line semimetal CaSb_2 Weiyin Duan,^{1,2} Jiawen Zhang,^{1,2} Rohit Kumar ^{1,2} Hang Su,^{1,2} Yuwei Zhou,^{1,2} Zhiyong Nie,^{1,2} Ye Chen,^{1,2} Michael Smidman ^{1,2} Chao Cao ^{1,2} Yu Song ^{1,2,*} and Huiqiu Yuan ^{1,2,3,4,†}¹*Center for Correlated Matter and School of Physics, Zhejiang University, Hangzhou 310058, China*²*Zhejiang Province Key Laboratory of Quantum Technology and Devices, Department of Physics, Zhejiang University, Hangzhou 310058, China*³*State Key Laboratory of Silicon Materials, Zhejiang University, Hangzhou 310058, China*⁴*Collaborative Innovation Center of Advanced Microstructures, Nanjing 210093, China*

(Received 28 July 2022; revised 4 October 2022; accepted 6 December 2022; published 22 December 2022)

CaSb_2 is a topological nodal-line semimetal that becomes superconducting below 1.6 K, providing an ideal platform to investigate the interplay between topologically nontrivial electronic bands and superconductivity. In this work, we investigated the superconducting order parameter of CaSb_2 by measuring its magnetic penetration depth change $\Delta\lambda(T)$ down to 0.07 K, using a tunnel diode oscillator based technique. Well inside the superconducting state, $\Delta\lambda(T)$ shows an exponential activated behavior, and provides direct evidence for a nodeless superconducting gap. By analyzing the temperature dependence of the penetration depth, the superfluid density and the electronic specific heat, we find both can be consistently described by a two-gap *s*-wave model, in line with the presence of multiple Fermi surfaces associated with distinct Sb sites in this compound. These results demonstrate fully gapped superconductivity in CaSb_2 and constrain the allowed pairing symmetry.

DOI: [10.1103/PhysRevB.106.214521](https://doi.org/10.1103/PhysRevB.106.214521)**I. INTRODUCTION**

Topological superconductors (TSCs) have drawn major research efforts in recent years, due to both fundamental interest in the unconventional superconducting state and the potential for applications in topological quantum computation [1–4]. One route towards discovering TSCs is by turning materials with topologically nontrivial band structures into superconductors via various tuning parameters. For instance, superconductivity in $\text{Cu}_x\text{Bi}_2\text{Se}_3$ is realized by intercalating Cu into the topological insulator Bi_2Se_3 [5–8], whereas in the type-II Weyl semimetal MoTe_2 and the three-dimensional Dirac semimetal Cd_3As_2 , superconductivity can be induced through the application of hydrostatic pressure [9–12]. Alternatively, intrinsic TSCs may be realized in topological semimetals (TSMs) that exhibit superconducting ground states, without additional tuning. In addition, such superconducting TSMs offer a fertile ground to probe the interplay between various topologically protected states and superconductivity [13].

Nodal-line semimetals, in which band crossings form closed loops (nodal lines) rather than discrete points (as in Dirac or Weyl semimetals) in momentum space [14–16], have received significant attention recently. Due to their unique nontrivial electronic topology, nodal-line semimetals can exhibit long-range Coulomb interactions, a large surface polarization charge [17–19], and torus-shaped Fermi surfaces (FSs) when the nodal line is close to the Fermi energy E_F .

If odd-parity superconductivity in a nodal-line semimetal is dominantly induced on such torus-shaped FSs, topological superconductivity can be realized [20]. Therefore, nodal-line semimetals with superconducting ground states are promising TSC candidates. However, since the nodal line can easily become gapped due to spin-orbit coupling (SOC), an additional symmetry is required to protect the nodal-line against SOC [21,22]. As a result of these constraints, reports on superconducting nodal-line semimetals have been limited thus far [23–25].

Recently, CaSb_2 was found to be a Dirac nodal-line semimetal with a superconducting ground state, and has been the focus of much interest [26–29]. A nonsaturating giant magnetoresistance, and a metal-to-insulator-like transition followed by a saturating behavior are observed in transport measurements on CaSb_2 under applied magnetic fields [26,27]. These observations are similar to those found in other TSMs [30–38], and can be ascribed to Dirac electrons from the Dirac nodal lines in CaSb_2 . In addition, the Dirac nodal lines in CaSb_2 are protected by the nonsymmorphic symmetry, and are thus robust against SOC. These unique properties make CaSb_2 an excellent candidate to look for topological superconductivity and investigate the interplay between nontrivial electronic band topology and superconductivity.

To make progress in these directions, an important property that needs to be experimentally clarified is the nature of the superconducting order parameter in CaSb_2 . Theoretically, symmetry enforced nodal lines were suggested to be present in CaSb_2 if the gap symmetry belongs to the B_g representation [39]. Experimentally, specific heat measurements down to 0.22 K in CaSb_2 single crystal uncover clear deviations

*Corresponding author: yusong_phys@zju.edu.cn†Corresponding author: hqyuan@zju.edu.cn

from expectations for a simple BCS superconductor [27], and the superconducting transition temperature T_c of pressurized CaSb_2 forms a peak around 3.1 GPa [40], which can be attributed to unconventional pairing. While these results suggest CaSb_2 may harbor an unconventional superconducting state, $^{121/123}\text{Sb}$ -nuclear quadrupole resonance measurements revealed a coherence peak below T_c in polycrystalline samples of CaSb_2 , which instead suggests conventional s -wave superconductivity [41]. To resolve these differences and elucidate the superconducting order parameter of CaSb_2 , experiments highly sensitive to low-energy electronic excitations inside the superconducting state are needed.

In this work, the magnetic penetration depth and electronic specific heat of CaSb_2 single crystals were measured to probe its superconducting gap structure. The temperature dependence of the magnetic penetration depth change $\Delta\lambda(T)$ was measured down to 0.07 K, using a technique based on the tunnel diode oscillator (TDO), which is extremely sensitive to low-energy electronic excitations. The $\Delta\lambda(T)$ of CaSb_2 exhibits an exponential behavior and flattens at low temperatures, evidencing a nodeless superconducting ground state. By analyzing the electronic specific heat and the superfluid density derived from $\Delta\lambda(T)$, we find both results are consistently captured by a two-gap s -wave model. Our findings provide evidence for nodeless multigap superconductivity in the nodal-line semimetal CaSb_2 .

II. EXPERIMENTAL DETAILS

Single crystals of CaSb_2 were grown using the Sb self-flux method, as described in Ref. [27]. The electrical resistivity $\rho(T)$ was measured in a ^3He cryostat using the four probe method. The specific heat was measured in a Quantum Design Physical Property Measurement System (PPMS) with a ^3He insert. The temperature dependence of the magnetic penetration depth shift $\Delta\lambda(T) = \lambda(T) - \lambda(0)$ was measured using a TDO operating at about 7 MHz [42,43]. $\Delta\lambda(T)$ can be obtained from the TDO frequency shift $\Delta f(T)$ through $\Delta\lambda(T) = G\Delta f(T)$, where G is the calibration factor determined from the geometry of the coil and the sample [44]. TDO measurements down to 0.35 and 0.07 K were, respectively, carried out in ^3He and dilution refrigerators. Two samples were separately mounted on a sapphire rod and inserted into the TDO coil without contact. The rod is connected to a copper stage, where the thermometer is mounted. The coil of the TDO generates a very tiny ac magnetic field ($\approx 2 \mu\text{T}$) along the c axis, which is much smaller than the lower critical field of CaSb_2 ($H_{c1} \approx 3.9 \text{ mT}$ [27]), ensuring the samples are in the full Meissner state once cooled slightly below T_c .

III. EXPERIMENTAL RESULTS AND DISCUSSION

The inset of Fig. 1 shows the electrical resistivity $\rho(T)$ of CaSb_2 from 300 down to 0.5 K, revealing a metallic normal state with a residual resistivity of about $1.2 \mu\Omega \text{ cm}$ and a large residual resistivity ratio (RRR) of $\rho(300 \text{ K})/\rho(1.6 \text{ K}) = 95$, comparable with previous works [27,41]. Figure 1 zooms into $\rho(T)$ below 2 K, revealing a clear superconducting transition that onsets around 1.6 K and offsets around 1.46 K. Both the

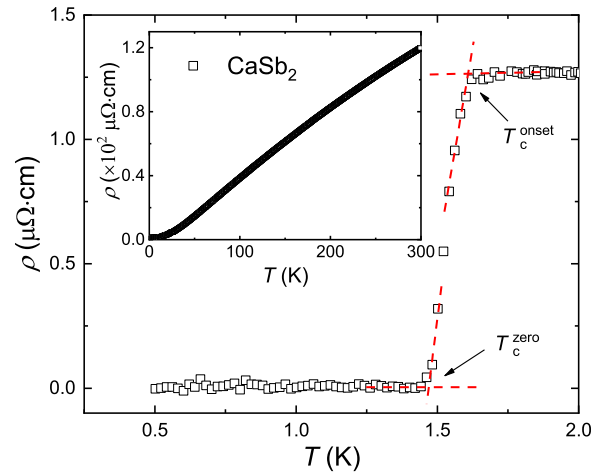


FIG. 1. The temperature dependence of the low temperature electrical resistivity $\rho(T)$ for CaSb_2 , with a sharp superconducting transition at 1.6 K. The inset shows $\rho(T)$ from 0.5 K up to 300 K.

large RRR and the small transition width (0.14 K) demonstrate the samples used in this work are of high quality.

The total specific heat $C(T)/T$ of CaSb_2 is shown in the inset of Fig. 2, with a clear superconducting jump around $T_c = 1.6 \text{ K}$ which indicates the appearance of bulk superconductivity, consistent with electrical resistivity measurements. In the normal state, the specific heat can be modeled using $C(T)/T = \gamma + \beta T^2 + \delta T^4$ (solid red line in the inset of Fig. 2), with $\gamma = 1.71 \text{ mJ mol}^{-1}\text{K}^{-2}$, $\beta = 0.507 \text{ mJ mol}^{-1}\text{K}^{-4}$ and $\delta = 0.0079 \mu\text{J mol}^{-1}\text{K}^{-6}$. γ is the Sommerfeld coefficient, and the other two parameters characterize the phonon contribution to the specific heat. After subtracting the phonon contribution, the electronic specific heat $C_{\text{el}}(T)/\gamma T$ is obtained, as shown in the main panel of Fig. 2. We find that neither a simple BCS model, nor a p -wave model with point nodes, nor a d -wave model with line nodes, can

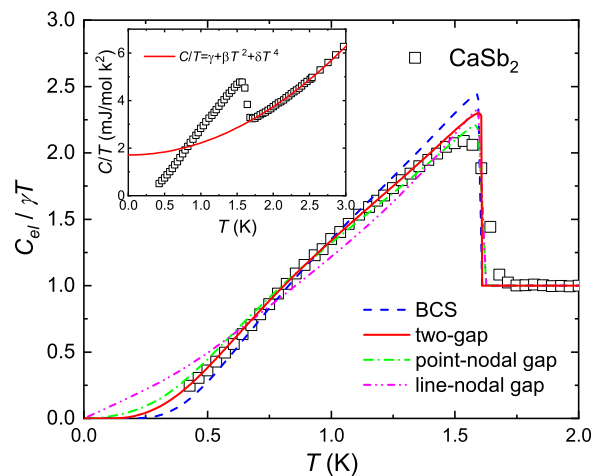


FIG. 2. The electronic specific heat $C_{\text{el}}(T)/\gamma T$ for CaSb_2 , with a clear superconducting transition at $T_c = 1.6 \text{ K}$. The solid, dashed, dashed-dotted, and dashed-dot-dotted lines are respectively fits to a two-gap s -wave model, a simple BCS model, a p -wave model with point nodes, and a d -wave model with line nodes. The inset shows the total specific heat $C(T)/T$, fit to $C(T)/T = \gamma + \beta T^2 + \delta T^4$ in the normal state.

TABLE I. Fit parameters for the two-gap BCS model obtained by fitting the electronic specific heat $C_{el}(T)$, the penetration depth $\Delta\lambda(T)$, and the superfluid density $\rho_s(T)$.

	$\Delta_1(0)/k_B T_c$	$\Delta_2(0)/k_B T_c$	x
$C_{el}(T)$	1.77	0.88	0.85
$\Delta\lambda(T)$	1.8	0.81	0.85
$\rho_s(T)$	1.85	0.84	0.86

capture the temperature evolution of $C_{el}(T)/\gamma T$, consistent with Ref. [27]. On the other hand, a two-gap BCS model gives an excellent description of the experimental data over the full temperature range (solid red line). The fit gap values are $\Delta_1(0) = 1.77k_B T_c$ and $\Delta_2(0) = 0.88k_B T_c$, with respective weights of 85% and 15% (Table I).

To further probe the superconducting gap structure of CaSb_2 , we measured the magnetic penetration depth change $\Delta\lambda(T)$ of two different samples, which are converted from the frequency shift $\Delta f(T)$ with respective calibration constants $G = 11.0 \text{ \AA/Hz}$ and 12.2 \AA/Hz . In Fig. 3, $\Delta\lambda(T)$ for CaSb_2 from 2.5 K down to 0.07 K is shown in the inset, with a clear reduction upon cooling around $T_c = 1.6$ K due to superconductivity, consistent with electrical resistivity and specific heat measurements in Figs. 1 and 2. In the main panel of Fig. 3, $\Delta\lambda(T)$ is zoomed in to focus on its behavior well below T_c . Measurements for the two CaSb_2 samples show excellent agreement between each other.

Following the method in Ref. [45], using the Sommerfeld coefficient of $\gamma = 1.71 \text{ mJ mol}^{-1} \text{ K}^{-2}$, the residual resistivity of $1.2 \mu\Omega \text{ cm}$ obtained above, and a coherence length of $\xi_0 = 116 \text{ nm}$ from Ref. [27], we estimate the mean free path in CaSb_2 to be 947 nm. This is much larger than the coherence length, indicating that the sample is in the clean limit.

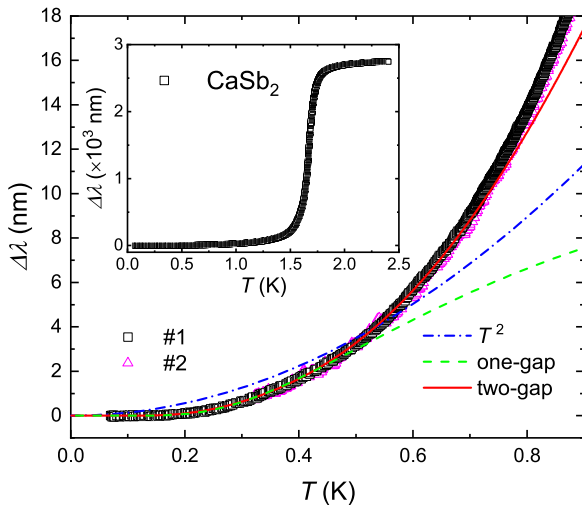


FIG. 3. The change of the magnetic penetration depth $\Delta\lambda(T)$, measured for two samples (#1 and #2). The dash-dotted, dashed and solid lines are, respectively, fits to the T^2 model, Eq. (1) and Eq. (5) at low temperature. The inset shows $\Delta\lambda(T)$ from 2.5 K down to 0.07 K, with a clear superconducting transition observed around 1.6 K, consistent with electrical resistivity and heat capacity measurements.

In the clean limit, the magnetic penetration depth at low temperatures is expected to exhibit a T -linear behavior in superconductors with line nodes, and a T^2 behavior in superconductors with point nodes. As shown in Fig. 3, $\Delta\lambda(T)$ clearly deviates from a T -linear behavior, and the T^2 model also fails to capture $\Delta\lambda(T)$, indicating that there are no nodes in the superconducting gap structure of CaSb_2 .

For an isotropic one-gap Bardeen-Cooper-Schrieffer (BCS) model, the penetration depth at $T \ll T_c$ can be approximated by

$$\Delta\lambda(T) = \lambda(T) - \lambda(0) \approx \lambda(0) \sqrt{\frac{\pi \Delta(0)}{2k_B T}} \exp\left(-\frac{\Delta(0)}{k_B T}\right), \quad (1)$$

where $\lambda(0)$ and $\Delta(0)$ are the magnitude of the penetration depth and the superconducting gap at zero temperature [46]. It can be seen that in contrast to the T^2 model, the one-gap BCS model gives an excellent description of $\Delta\lambda(T)$ in Fig. 3 at low temperatures ($T < 0.25T_c$), providing strong evidence for nodeless superconductivity in CaSb_2 . The derived superconducting gap is found to be $\Delta(0) = 0.9k_B T_c$, which is significantly smaller than the weak-coupling limit of $\Delta(0) = 1.76k_B T_c$, and can arise from the presence of multiple superconducting gaps. This conclusion is corroborated by the excellent agreement between the fit gap value from low-temperature $\Delta\lambda(T)$ and the small gap obtained in specific heat measurements.

The total superfluid density can be considered as the sum of two independent superconducting fluids taken as two independent parallel conduction channels (no cross terms) of equivalent carriers ($m_1 = m_2 = m^*$) [47–50]:

$$n_s(T) = n_{s1}(T) + n_{s2}(T), \quad (2)$$

where n_{s1} and n_{s2} are the superfluid densities of the first and the second superconducting bands, respectively.

Equation (2) can be recast in terms of the magnetic penetration depth, which allows the normalized superfluid density $\rho_s(T)$ to be determined via

$$\begin{aligned} \rho_s(T) &= \frac{\lambda^2(0)}{\lambda^2(T)} \\ &= x \frac{\lambda_1^2(0)}{\lambda_1^2(T)} + (1-x) \frac{\lambda_2^2(0)}{\lambda_2^2(T)} \\ &= x\rho_{s1} + (1-x)\rho_{s2}, \end{aligned} \quad (3)$$

where $\lambda_i(T)$ and $\rho_i(T)$ ($i = 1, 2$) are the magnetic penetration depth and the normalized superfluid density for each of the two bands. The relative weights of the two bands' contribution to ρ_s are represented by $x = \frac{\lambda_1^2(0)}{\lambda_1^2(0) + \lambda_2^2(0)}$ and $(1-x) = \frac{\lambda_2^2(0)}{\lambda_1^2(0) + \lambda_2^2(0)}$.

When $T \ll T_c$, $\lambda_i(T)/\lambda_i(0)$ can be approximated using Eq. (1):

$$\frac{\lambda_i(T)}{\lambda_i(0)} \approx 1 + \sqrt{\frac{\pi \Delta_i(0)}{2k_B T}} \exp\left(-\frac{\Delta_i(0)}{k_B T}\right) \equiv g(\Delta_i(0), T). \quad (4)$$

Substituting Eq. (4) into Eq. (3), an explicit expression for $\Delta\lambda(T)$ is found to be

$$\Delta\lambda(T) = \lambda(0) \left\{ \sqrt{\frac{1}{\frac{x}{[g(\Delta_1(0), T)]^2} + \frac{1-x}{[g(\Delta_2(0), T)]^2}} - 1} \right\}. \quad (5)$$

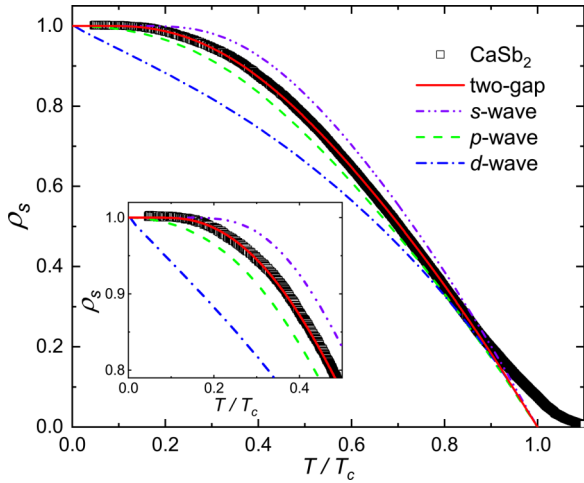


FIG. 4. Normalized superfluid density $\rho_s(T)$ for sample #1 as a function of the reduced temperature T/T_c , obtained using $\lambda(0) = 89.5$ nm. The solid, dashed-dot-dotted, dashed, and dashed-dotted lines are, respectively, fits to models with two s -wave gaps, a single s -wave gap, a p -wave gap, and a d -wave gap. The inset zooms into the low temperature region of $\rho_s(T)$.

In Fig. 3, the experimental data $\Delta\lambda(T)$ were analyzed using Eq. (5) from the lowest measured temperature up to $0.45T_c$, with $\lambda(0)$, x , $\Delta_1(0)$ and $\Delta_2(0)$ as fitting parameters. $\lambda(0)$ is found to be 92 nm, and the values of $\Delta_1(0)$, $\Delta_2(0)$ and x are listed in Table I, which are in good agreement with values obtained from the analysis of $C_{el}(T)$.

To further elucidate the superconductivity in CaSb_2 , the superfluid density is calculated through $\rho_s(T) = [\lambda(0)/\lambda(T)]^2$ (Fig. 4), using $\lambda(0) = 92$ nm. The obtained ρ_s is fit to several different models of the superconducting gap function Δ_k , which determines ρ_s through

$$\rho_s(T) = 1 + 2 \left\langle \int_{\Delta}^{\infty} \frac{E dE}{\sqrt{E^2 - \Delta_k^2}} \frac{\partial f(E, T)}{\partial E} \right\rangle_{\text{FS}}, \quad (6)$$

where $f(E, T) = [1 + \exp(E/k_B T)]^{-1}$ is the Fermi-Dirac distribution and $\langle \dots \rangle_{\text{FS}}$ represents an average over the Fermi surface [46]. The gap function is defined as $\Delta_k(T) = \Delta(T)g_k$, where g_k represents the angular dependence of the gap structure, with $g_k = 1, \sin\theta$ and $\cos 2\phi$, corresponding to s -, p -, and d -wave superconducting gaps (θ is the polar angle and ϕ is the azimuthal angle), respectively. The temperature dependence of $\Delta(T)$ is approximated as [47]:

$$\Delta(T) = \Delta(0) \tanh\{1.82[1.018(T_c/T - 1)]^{0.51}\}, \quad (7)$$

where $\Delta(0)$ represents the gap magnitude at zero temperature.

As shown in Fig. 4, the experimental normalized superfluid density is not fully captured by any of the s -, p -, and d -wave models. On the other hand, we find that a two-gap BCS model [Eq. (3)] describes the data well over the entire temperature range [solid line in Fig. 4(a)]. The fit parameters are listed in Table I, in good agreement with the fit of $\Delta\lambda(T)$ to Eq. (5). This suggests that the set of parameters $\lambda(0)$, $\Delta_1(0)$, $\Delta_2(0)$ and x not only successfully describes the behavior of $\Delta\lambda(T)$ for $T \lesssim T_c/2$, but also reproduces $\rho_s(T)$ up to T_c .

Our conclusion of a multigap superconducting state in CaSb_2 agrees with upper critical field measurements [29], and is consistent with the presence of multiple Fermi surfaces found in electronic structure calculations, quantum oscillations, and angle-resolved photoemission spectroscopy measurements [26,27,39,41,51]. While the electronic bands near the Fermi level are dominated by contributions from Sb states, the electron bands crossing the Fermi level along $\Gamma - Z$ and the hole band centered around the Γ point are associated with Sb states on distinct sites. Therefore, the presence of multiple Fermi surfaces originating from different orbital states provides a natural explanation for the phenomenology of multi-gap nodeless superconductivity revealed in our measurements.

As discussed in Ref. [39], since the space group of CaSb_2 is $P2_1/m$ (space group No. 11), the associated symmetries include the inversion symmetry I , the two-fold screw axis S_{2y} , and the mirror symmetry M_y . These symmetries give rise to four one-dimensional representations for the superconducting order parameter: B_g ($\chi_I = +1, \chi_{M_y} = -1$), A_g ($\chi_I = +1, \chi_{M_y} = +1$), B_u ($\chi_I = -1, \chi_{M_y} = +1$) and A_u ($\chi_I = -1, \chi_{M_y} = -1$), where χ_X represents the sign of the superconducting order parameter under the symmetry operation X . When weak coupling pairing is assumed, the superconducting phases corresponding to different representations can be deduced through the method in Ref. [39]. In particular, for a superconducting order parameter belonging to the B_g representation, it is predicted that CaSb_2 has a topologically protected nodal-line superconducting gap structure on the $k_y = 0$ plane. On the other hand, for order parameters belonging to the A_u , B_u , and A_g representations, there are no symmetry-enforced nodal structures. Superconductivity is topologically nontrivial for the A_u and B_u representations, but topologically trivial for the A_g representation. From our experimental results, the superconducting gap structure of CaSb_2 is demonstrated to be nodeless, which excludes the B_g pairing symmetry.

In addition, for a topological nodal-line semimetal such as CaSb_2 , there may be degenerate two-dimensional energy bands that are localized on surfaces parallel to the nodal loop, which are called “drumhead bands” [14,19,52,53]. It is then possible to generate topological superconductivity from these surface states through the proximity effect via superconductivity in the bulk [1,2,6,54]. In this scenario, helical spin-polarized electrons on the topological surface state can pair with $p_x + ip_y$ symmetry and realize bound Majorana fermions with non-Abelian statistics. So far, reports on superconductors with nodal lines in the normal state are limited [23–25], and CaSb_2 offers a rare opportunity to search for topological superconductivity in a nodal-line semimetal. Further experiments that look for topological surface states and Majorana zero modes in CaSb_2 are needed.

IV. CONCLUSION

In conclusion, we investigated the superconducting order parameter of the topological nodal-line semimetal CaSb_2 through magnetic penetration depth measurements down to 0.07 K. Clear exponential behaviors below $T < T_c$ evidence nodeless superconductivity in CaSb_2 , and quantitative

analysis of the penetration depth, the superfluid density and the electronic specific heat suggest the superconducting gap structure of CaSb_2 can be described by a two-gap BCS model, consistent with the presence of multiple Fermi surfaces. These results demonstrate the absence of nodes in the superconducting order parameter of CaSb_2 and exclude the B_g representation. Further work is needed to clarify whether CaSb_2 realizes topological superconductivity on the surface.

ACKNOWLEDGMENTS

This work was supported by the National Natural Science Foundation of China (Grant No. 11974306 and No. 12034017), the Key R&D Program of Zhejiang Province, China (Grant No. 2021C01002), the National Key R&D Program of China (Grant No. 2022YFA1402200), and Zhejiang Provincial Natural Science Foundation of China (R22A0410240).

-
- [1] X.-L. Qi and S.-C. Zhang, Topological insulators and superconductors, *Rev. Mod. Phys.* **83**, 1057 (2011).
- [2] M. Sato and Y. Ando, Topological superconductors: A review, *Rep. Prog. Phys.* **80**, 076501 (2017).
- [3] C. Nayak, S. H. Simon, A. Stern, M. Freedman, and S. Das Sarma, Non-Abelian anyons and topological quantum computation, *Rev. Mod. Phys.* **80**, 1083 (2008).
- [4] A. Y. Kitaev, Unpaired majorana fermions in quantum wires, *Phys. Usp.* **44**, 131 (2001).
- [5] Y. S. Hor, A. J. Williams, J. G. Checkelsky, P. Roushan, J. Seo, Q. Xu, H. W. Zandbergen, A. Yazdani, N. P. Ong, and R. J. Cava, Superconductivity in $\text{Cu}_x\text{Bi}_2\text{Se}_3$ and its Implications for Pairing in the Undoped Topological Insulator, *Phys. Rev. Lett.* **104**, 057001 (2010).
- [6] M. Z. Hasan and C. L. Kane, Colloquium: Topological insulators, *Rev. Mod. Phys.* **82**, 3045 (2010).
- [7] L. A. Wray, S.-Y. Xu, Y. Xia, Y. S. Hor, D. Qian, A. V. Fedorov, H. Lin, A. Bansil, R. J. Cava, and M. Z. Hasan, Observation of topological order in a superconducting doped topological insulator, *Nat. Phys.* **6**, 855 (2010).
- [8] R. Tao, Y.-J. Yan, X. Liu, Z.-W. Wang, Y. Ando, Q.-H. Wang, T. Zhang, and D.-L. Feng, Direct Visualization of the Nematic Superconductivity in $\text{Cu}_x\text{Bi}_2\text{Se}_3$, *Phys. Rev. X* **8**, 041024 (2018).
- [9] Y. Qi, P. G. Naumov, M. N. Ali, C. R. Rajamathi, W. Schnelle, O. Barkalov, M. Hanfland, S.-C. Wu, C. Shekhar, Y. Sun, V. Süß, M. Schmidt, U. Schwarz, E. Pippel, P. Werner, R. Hillebrand, T. Förster, E. Kampert, S. Parkin, R. J. Cava *et al.*, Superconductivity in Weyl semimetal candidate $T_d\text{-MoTe}_2$, *Nat. Commun.* **7**, 11038 (2016).
- [10] Z. Guguchia, F. von Rohr, Z. Shermadini, A. T. Lee, S. Banerjee, A. R. Wieteska, C. A. Marianetti, B. A. Frandsen, H. Luetkens, Z. Gong, S. C. Cheung, C. Baines, A. Shengelaya, G. Taniashvili, A. N. Pasupathy, E. Morenzoni, S. J. L. Billinge, A. Amato, R. J. Cava, R. Khasanov *et al.*, Signatures of the topological s^{+-} superconducting order parameter in the type-II Weyl semimetal MoTe_2 , *Nat. Commun.* **8**, 1082 (2017).
- [11] L. He, Y. Jia, S. Zhang, X. Hong, C. Jin, and S. Li, Pressure-induced superconductivity in the three-dimensional topological dirac semimetal Cd_3As_2 , *npj Quantum Mater.* **1**, 16014 (2016).
- [12] S. Kobayashi and M. Sato, Topological Superconductivity in Dirac Semimetals, *Phys. Rev. Lett.* **115**, 187001 (2015).
- [13] X. Luo, D. F. Shao, Q. L. Pei, J. Y. Song, L. Hu, Y. Y. Han, X. B. Zhu, W. H. Song, W. J. Lu, and Y. P. Sun, Superconductivity in CaSn_3 single crystals with a AuCu_3 -type structure, *J. Mater. Chem. C* **3**, 11432 (2015).
- [14] A. A. Burkov, M. D. Hook, and L. Balents, Topological nodal semimetals, *Phys. Rev. B* **84**, 235126 (2011).
- [15] X. D. H. W. Rui Yu, Zhong Fang, Topological nodal line semimetals predicted from first-principles calculations, *Front. Phys.* **12**, 127202 (2017).
- [16] T. Bzdušek, Q. Wu, A. Rüegg, M. Sigrist, and A. A. Soluyanov, Nodal-chain metals, *Nature (London)* **538**, 75 (2016).
- [17] Y. Huh, E.-G. Moon, and Y. B. Kim, Long-range Coulomb interaction in nodal-ring semimetals, *Phys. Rev. B* **93**, 035138 (2016).
- [18] M. Hirayama, R. Okugawa, T. Miyake, and S. Murakami, Topological Dirac nodal lines and surface charges in fcc alkaline earth metals, *Nat. Commun.* **8**, 14022 (2017).
- [19] S. T. Ramamurthy and T. L. Hughes, Quasitopological electromagnetic response of line-node semimetals, *Phys. Rev. B* **95**, 075138 (2017).
- [20] H. Shapourian, Y. Wang, and S. Ryu, Topological crystalline superconductivity and second-order topological superconductivity in nodal-loop materials, *Phys. Rev. B* **97**, 094508 (2018).
- [21] C. Fang, Y. Chen, H.-Y. Kee, and L. Fu, Topological nodal line semimetals with and without spin-orbital coupling, *Phys. Rev. B* **92**, 081201(R) (2015).
- [22] Y. X. Zhao and A. P. Schnyder, Nonsymmorphic symmetry-required band crossings in topological semimetals, *Phys. Rev. B* **94**, 195109 (2016).
- [23] G. Bian, T.-R. Chang, R. Sankar, S.-Y. Xu, H. Zheng, T. Neupert, C.-K. Chiu, S.-M. Huang, G. Chang, I. Belopolski, D. S. Sanchez, M. Neupane, N. Alidoust, C. Liu, B. Wang, C.-C. Lee, H.-T. Jeng, C. Zhang, Z. Yuan, S. Jia *et al.*, Topological nodal-line fermions in spin-orbit metal PbTaSe_2 , *Nat. Commun.* **7**, 10556 (2016).
- [24] T. Shang, S. K. Ghosh, M. Smidman, D. J. Gawryluk, C. Baines, A. Wang, W. Xie, Y. Chen, M. O. Ajeesh, M. Nicklas, E. Pomjakushina, M. Medarde, M. Shi, J. F. Annett, H. Yuan, J. Quintanilla, and T. Shiroka, Spin-triplet superconductivity in Weyl nodal-line semimetals, *npj Quantum Mater.* **7**, 35 (2022).
- [25] L. Li, G.-X. Zhi, Q. Zhu, C. Wu, Z. Yang, J. Du, J. Yang, B. Chen, H. Wang, C. Cao, and M. Fang, Superconductivity in the nodal-line compound $\text{La}_3\text{Pt}_3\text{Bi}_4$, *Phys. Rev. Res.* **4**, L032004 (2022).
- [26] K. Funada, A. Yamakage, N. Yamashina, and H. Kageyama, Spinorbit-coupling-induced type-I/type-II dirac nodal-line metal in nonsymmorphic CaSb_2 , *J. Phys. Soc. Jpn.* **88**, 044711 (2019).
- [27] M. Oudah, J. Bannies, D. A. Bonn, and M. C. Aronson, Superconductivity and quantum oscillations in single crystals of the compensated semimetal CaSb_2 , *Phys. Rev. B* **105**, 184504 (2022).
- [28] A. Ikeda, M. Kawaguchi, S. Koibuchi, T. Hashimoto, T. Kawakami, S. Yonezawa, M. Sato, and Y. Maeno, Supercon-

- ductivity in the nonsymmorphic line-nodal compound CaSb_2 , *Phys. Rev. Mater.* **4**, 041801(R) (2020).
- [29] A. Ikeda, S. R. Saha, D. Graf, P. Saraf, D. S. Sokratov, Y. Hu, H. Takahashi, S. Yamane, A. Jayaraj, J. Ślawińska, M. B. Nardelli, S. Yonezawa, Y. Maeno, and J. Paglione, Quasi-two-dimensional Fermi surface of superconducting line-nodal metal CaSb_2 , *Phys. Rev. B* **106**, 075151 (2022).
- [30] X. Huang, L. Zhao, Y. Long, P. Wang, D. Chen, Z. Yang, H. Liang, M. Xue, H. Weng, Z. Fang, X. Dai, and G. Chen, Observation of the Chiral-Anomaly-Induced Negative Magnetoresistance in 3D Weyl Semimetal TaAs, *Phys. Rev. X* **5**, 031023 (2015).
- [31] Y. Li, L. Li, J. Wang, T. Wang, X. Xu, C. Xi, C. Cao, and J. Dai, Resistivity plateau and negative magnetoresistance in the topological semimetal TaSb₂, *Phys. Rev. B* **94**, 121115(R) (2016).
- [32] F. F. Tafti, Q. D. Gibson, S. K. Kushwaha, N. Haldolaarachchige, and R. J. Cava, Resistivity plateau and extreme magnetoresistance in LaSb, *Nat. Phys.* **12**, 272 (2016).
- [33] X. Yuan, Z. Yan, C. Song, M. Zhang, Z. Li, C. Zhang, Y. Liu, W. Wang, M. Zhao, Z. Lin, T. Xie, J. Ludwig, Y. Jiang, X. Zhang, C. Shang, Z. Ye, J. Wang, F. Chen, Z. Xia, D. Smirnov *et al.*, Chiral Landau levels in Weyl semimetal NbAs with multiple topological carriers, *Nat. Commun.* **9**, 1854 (2018).
- [34] Y. Jiang, Z. Dun, S. Moon, H. Zhou, M. Koshino, D. Smirnov, and Z. Jiang, Landau quantization in coupled Weyl points: A case study of semimetal NbP, *Nano Lett.* **18**, 7726 (2018).
- [35] Y.-Y. Lv, B.-B. Zhang, X. Li, S.-H. Yao, Y. B. Chen, J. Zhou, S.-T. Zhang, M.-H. Lu, and Y.-F. Chen, Extremely large and significantly anisotropic magnetoresistance in ZrSiS single crystals, *Appl. Phys. Lett.* **108**, 244101 (2016).
- [36] M. N. Ali, J. Xiong, S. Flynn, J. Tao, Q. D. Gibson, L. M. Schoop, T. Liang, N. Haldolaarachchige, M. Hirschberger, N. P. Ong, and R. J. Cava, Large, non-saturating magnetoresistance in WTe_2 , *Nature (London)* **514**, 205 (2014).
- [37] C. Shekhar, A. K. Nayak, Y. Sun, M. Schmidt, M. Nicklas, I. Leermakers, U. Zeitler, Y. Skourski, J. Wosnitza, Z. Liu, Y. Chen, W. Schnelle, H. Borrmann, Y. Grin, C. Felser, and B. Yan, Extremely large magnetoresistance and ultrahigh mobility in the topological Weyl semimetal candidate NbP, *Nat. Phys.* **11**, 645 (2015).
- [38] D. Chen, L. X. Zhao, J. B. He, H. Liang, S. Zhang, C. H. Li, L. Shan, S. C. Wang, Z. A. Ren, C. Ren, and G. F. Chen, Magnetotransport properties of the type-II Weyl semimetal candidate Ta₃S₂, *Phys. Rev. B* **94**, 174411 (2016).
- [39] S. Ono, H. C. Po, and K. Shiozaki, Z₂-enriched symmetry indicators for topological superconductors in the 1651 magnetic space groups, *Phys. Rev. Res.* **3**, 023086 (2021).
- [40] S. Kitagawa, K. Ishida, A. Ikeda, M. Kawaguchi, S. Yonezawa, and Y. Maeno, Peak in the superconducting transition temperature of the nonmagnetic topological line-nodal material CaSb_2 under pressure, *Phys. Rev. B* **104**, L060504 (2021).
- [41] H. Takahashi, S. Kitagawa, K. Ishida, M. Kawaguchi, A. Ikeda, S. Yonezawa, and Y. Maeno, S-wave superconductivity in the Dirac line-nodal material CaSb_2 , *J. Phys. Soc. Jpn.* **90**, 073702 (2021).
- [42] C. T. Van Degrift, Tunnel diode oscillator for 0.001 ppm measurements at low temperatures, *Rev. Sci. Instrum.* **46**, 599 (1975).
- [43] E. M. E. Chia, Penetration depth studies of unconventional superconductors, Ph.D. thesis, University of Illinois at Urbana Champaign, 2004.
- [44] R. Prozorov, R. W. Giannetta, A. Carrington, and F. M. Araujo-Moreira, Meissner-London state in superconductors of rectangular cross section in a perpendicular magnetic field, *Phys. Rev. B* **62**, 115 (2000).
- [45] T. P. Orlando, E. J. McNiff, S. Foner, and M. R. Beasley, Critical fields, Pauli paramagnetic limiting, and material parameters of Nb₃Sn and V₃Si, *Phys. Rev. B* **19**, 4545 (1979).
- [46] R. Prozorov and R. W. Giannetta, Magnetic penetration depth in unconventional superconductors, *Supercond. Sci. Technol.* **19**, R41 (2006).
- [47] A. Carrington and F. Manzano, Magnetic penetration depth of MgB₂, *Physica C* **385**, 205 (2003).
- [48] F. Bouquet, Y. Wang, R. A. Fisher, D. G. Hinks, J. D. Jorgensen, A. Junod, and N. E. Phillips, Phenomenological two-gap model for the specific heat of MgB₂, *Europhys. Lett.* **56**, 856 (2001).
- [49] R. Khasanov, A. Shengelaya, A. Maisuradze, F. L. Mattina, A. Bussmann-Holder, H. Keller, and K. A. Müller, Experimental Evidence for Two Gaps in the High-Temperature La_{1.83}Sr_{0.17}CuO₄ Superconductor, *Phys. Rev. Lett.* **98**, 057007 (2007).
- [50] R. Khasanov, D. V. Evtushinsky, A. Amato, H.-H. Klauss, H. Luetkens, C. Niedermayer, B. Büchner, G. L. Sun, C. T. Lin, J. T. Park, D. S. Inosov, and V. Hinkov, Two-Gap Superconductivity in Ba_{1-x}K_xFe₂As₂: A Complementary Study of the Magnetic Penetration Depth by Muon-Spin Rotation and Angle-Resolved Photoemission, *Phys. Rev. Lett.* **102**, 187005 (2009).
- [51] C.-W. Chuang, S. Souma, A. Moriya, K. Nakayama, A. Ikeda, M. Kawaguchi, K. Obata, S. R. Saha, H. Takahashi, S. Kitagawa, K. Ishida, K. Tanaka, M. Kitamura, K. Horiba, H. Kumigashira, T. Takahashi, S. Yonezawa, J. Paglione, Y. Maeno, and T. Sato, Fermiology of a topological line-nodal compound CaSb_2 and its implication to superconductivity: Angle-resolved photoemission study, *Phys. Rev. Mater.* **6**, 104203 (2022).
- [52] T. T. Heikkilä and G. E. Volovik, Dimensional crossover in topological matter: Evolution of the multiple Dirac point in the layered system to the flat band on the surface, *JETP Lett.* **93**, 59 (2011).
- [53] Y.-H. Chan, C.-K. Chiu, M. Y. Chou, and A. P. Schnyder, Ca₃P₂ and other topological semimetals with line nodes and drumhead surface states, *Phys. Rev. B* **93**, 205132 (2016).
- [54] L. Fu and C. L. Kane, Superconducting Proximity Effect and Majorana Fermions at the Surface of a Topological Insulator, *Phys. Rev. Lett.* **100**, 096407 (2008).